Effect of Ramped Oxygen Flow during Magnetron Sputtering on the Structural, Optical, and Photoelectrochemical Properties of WO_{3-x} Thin Films

Helen Caroline de Souza Barros [1,*], David Alexandro Graves [2], Benedito Donizeti Botan Neto[3], Rafael da Silva Leal[1], Marcilene Cristina Gomes[1], Douglas Marcel Gonçalves Leite[1], Elizabete Yoshie Kawachi[2], Rodrigo Savio Pessoa[1], Nicolas Martin[4], Argemiro Soares da Silva Sobrinho[1] and André Luis de Jesus Pereira [1,*]

[1]Laboratório de Plasmas e Processos—LPP, Instituto Tecnológico de Aeronáutica—ITA, São José dos Campos 12228-900, Brazil; rafaellealquimicamg@gmail.com (R.L.); marcilenecgomes@gmail.com (M.G.); leitedmg@gmail.com (D.L.) argemirosss@gmail.com (A.S.).

[2]Departamento de Química, Instituto Tecnológico de Aeronáutica—ITA, São José dos Campos 12228-900, Brazil; dvdagraves@gmail.com (D.G.); bete@ita.br (E.K.)

[3]Departamento de Física Aplicada-ICMUV, MALTA Consolider Team, Universitat de València, Valencia 46100, Spain; bebone@uv.es (B.N.)

[4]Université Marie et Louis Pasteur, SUPMICROTECH, CNRS, Institut FEMTO-ST, F-25000 Besançon, France; nicolas.martin@femto-st.fr (N.M.)

*Correspondence: helencssb@gmail.com (H.B.); andreljp@ita.br (A.P.)

Abstract

The growing need for sustainable energy sources to replace fossil fuels has led to the exploration of green hydrogen production. Photoelectrochemical (PEC) water splitting, utilizing photoanodes composed of semiconductors such as WO_3, presents a promising solution. In this work, WO_{3-x} thin films were deposited by DC reactive magnetron sputtering, and the effect of oxygen flow ramping during deposition on the films' structural, optical, and photoelectrochemical properties was investigated. The films exhibited the monoclinic γ-WO_3 phase, with changes in their structural properties observed through X-ray diffraction (XRD), Raman spectroscopy, and scanning electron microscopy (SEM). The optical properties, measured by transmittance, showed that films deposited under intermediate oxygen flows exhibited higher transparency and a more favorable bandgap for PEC applications. Electrochemical impedance spectroscopy (EIS) and cyclic voltammetry (CV) revealed enhanced charge transfer and photoactivity in samples with intermediate oxygen flow rates. The results suggest that oxygen vacancy engineering, combined with precise control of deposition conditions, significantly enhances the photoelectrochemical performance of WO_{3-x} films. The study also highlights the importance of post-deposition annealing conditions for optimizing the material's photoelectrochemical response.

Keywords: Tungsten oxide; n-type semiconductor; thin films; magnetron sputtering; photoelectrodes; Oxygen Flow Ramping

1. Introduction

The intensification of climate change, driven by the long-standing reliance on fossil fuels since the Industrial Revolution, compels a transition toward clean, scalable energy matrices. Owing to its abundance and carbon-free nature, solar energy is poised to play a central role; however, its intermittency necessitates efficient and cost-effective energy storage routes [1,2]. Among the alternatives, green hydrogen produced

by water splitting (WS) in photoelectrochemical (PEC) cells is particularly promising, as it converts photon energy into stable chemical energy stored in H–H bonds [3–5].

In PECs, photon absorption by a semiconductor (photoanode) generates electron–hole pairs whose separation and interfacial transfer drive the oxygen evolution reaction (OER) at the photoanode and the hydrogen evolution reaction (HER) at the counter electrode [6–8]. Thermodynamically, the cleavage of H_2O requires at least 1.23 eV per electron, while kinetic and resistive losses raise the practical threshold, imposing simultaneous requirements on: (i) a bandgap compatible with solar photon harvesting; (ii) band-edge alignment with the redox windows of OER/HER; (iii) efficient charge separation/extraction; and (iv) electrochemical stability in aqueous electrolytes [6–8]. The experimental milestone was established by Fujishima and Honda (1972) using TiO_2 as the photoanode [9]; however, the $E_g \approx 3.2$ eV of TiO_2 restricts absorption to the ultraviolet, motivating the search for semiconductors that are active under visible light [7,10].

Within this landscape, tungsten trioxide (WO_3) has been extensively explored as a photoanode owing to its stability in acidic media, well-defined crystalline structure, and compatibility with large-area deposition, especially by magnetron sputtering[11–13]. Structurally polymorphic (monoclinic, triclinic, orthorhombic, tetragonal, and cubic), its monoclinic phase is the most stable at room temperature [12,14]. Electronically, WO_3 is typically n-type with an indirect bandgap of ~2.6–2.8 eV; the valence band derives largely from O 2p orbitals and the conduction band from W 5d states, enabling the generation of holes active for OER under visible illumination [12,14–16]. Since Hodes et al. (1976) demonstrated WO_3 as a photoanode [17], many strategies have been developed to address its main limitations. These include a limited absorption range in the blue–green spectrum, an unsuitable conduction-band position for HER, and high carrier recombination [11,12,16]. Approaches such as nanotexturing, adding co-catalysts, creating heterostructures, doping, and especially defect engineering have been explored [18–23].

Among intrinsic defects, oxygen vacancies in WO_{3-x} critically modulate electronic and catalytic properties: they act as shallow donors, increase n-type conductivity, shift the Fermi level, and can introduce intragap states, broadening effective absorption [24–26]. On the other hand, excessive surface densities can act as recombination centers and potentially undermine operational stability, highlighting the importance of precise control over the density and spatial arrangement of oxygen vacancies, which is essential [24,27]. One effective method for controlling oxygen vacancies is DC magnetron sputtering, which allows for precise adjustments of the oxygen partial pressure during deposition, directly influencing stoichiometry and defect content [28–30]. Specifically, adjusting the O_2/Ar ratio in the plasma is a well-established method for synthesizing sub-stoichiometric WO_{3-x} films, modulating the concentration of oxygen vacancies and, consequently, the optical, electronic, and photoelectrochemical properties [31,32].

Several studies employ fixed O_2 flow conditions (e.g., 10%, 20%, or 40%) to produce comparative series and correlate the defect content with functional performance [32]. In addition, the Reactive Gas Pulsing Process (RGPP) introduces oxygen in periodic pulses, allowing for space-time control of plasma chemistry at the substrate surface and enabling layered architectures with alternating stoichiometry or tailored defect profiles [33,34]. In parallel with fixed or pulsed flow schemes, continuous modulation strategies throughout the entire deposition process have been less represented in the literature and may significantly influence the properties of the film.

In this study, we investigate WO_{3-x} thin films prepared by magnetron sputtering, utilizing a ramping of the O_2 flow during deposition, intending to generate an oxygen gradient across the film thickness. Compared to traditional fixed or pulsed methods, this approach is, as far as we know, rarely documented. We perform morphological, structural, optical, and photoelectrochemical analyses to understand how a graded defect distribution affects (i) absorption and charge transport, (ii) interfacial separation and extraction, and (iii) overall PEC performance. Our findings aim to guide the development of more efficient and stable WO_{3-x} photoanodes for sustainable hydrogen production.

2. Materials and Methods

2.1. Deposition of WO_{3-x} thin films by DC Magnetron Sputtering

Tungsten oxide thin films were deposited on glass, silicon (100), and fluorine-doped tin oxide (FTO) substrates. Before deposition, the substrates were pre-cleaned in an ultrasonic bath with acetone and ethanol for 10 minutes each to remove surface contaminants and ensure proper film adhesion.

The deposition process was performed using a DC reactive magnetron sputtering system, equipped with a 100 mm diameter tungsten target of 99% purity. Before deposition, the chamber was evacuated to a base pressure of approximately 10^{-6} torr using a turbomolecular pump backed by a mechanical pump to ensure a clean and controlled environment. A pre-sputtering step was then carried out for 5 minutes with the shutter closed, in a pure argon atmosphere, to remove residual contamination from the tungsten target surface and prevent oxidation or poisoning. The subsequent deposition was performed under controlled conditions: a fixed DC power of 150 W, an argon flow of 10 sccm, a deposition time of 60 minutes, and ambient substrate temperature.

To implement oxygen flow ramping during WO_{3-x} deposition, oxygen flow was gradually increased from 0 to 10 sccm using a dynamic gas flow controller. The flow was adjusted in steps, starting at 2, 4, 6, and 8 sccm, reaching a maximum of 10 sccm at the end of the 60-minute process. Throughout the experiments, the oxygen flow was monitored at 5-minute intervals, allowing for the identification of the ramp profile during deposition (**Figure 1**). The control sample (WO_{3-x}-10) maintained a constant oxygen flow of 10 sccm throughout the process (**Figure 1**).

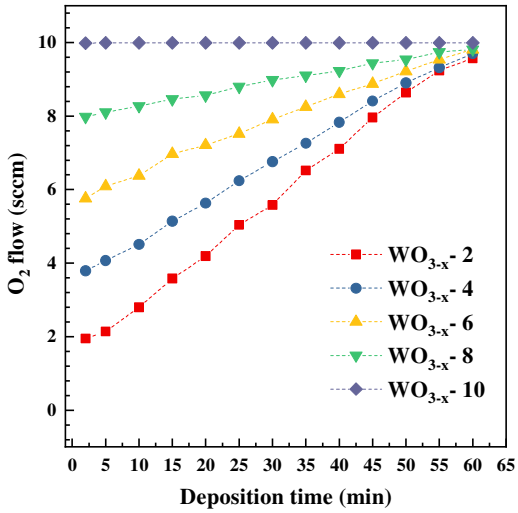

Figure 1 - Oxygen flow ramping profiles during WO_{3-x} thin film deposition by DC reactive magnetron sputtering. The control sample (WO_{3-x}-10) was deposited under a constant 10 sccm oxygen flow.

After deposition, the samples were heat-treated for 2 hours at 450°C, with a heating rate of 1°C/min in an ambient atmosphere. The resulting samples were labeled as WO_{3-x}-2, WO_{3-x}-4, WO_{3-x}-6, WO_{3-x}-8, and WO_{3-x}-10, corresponding to the initial oxygen flow in sccm used during deposition.

2.2 Characterization Techniques

The samples were characterized using various techniques to evaluate their structural, optical, and surface properties, thereby confirming the photoelectrochemical analyses. X-ray diffraction (XRD) analyses were performed with a PANalytical Empyrean diffractometer operating at 40 kV and 40 mA, equipped with a Cu Kα radiation source (λ = 0.15418 nm). Diffraction patterns were collected over a 2θ range from 20° to 90°, using a fixed divergence slit of 1/2°, a 10 mm mask, and a step size of 0.013° with a counting time of 0.013 seconds per step. Phase identification was achieved through Le Bail refinement with HighScore Plus software (Malvern PANalytical) [35], enabling precise fitting of diffraction profiles and confirmation of crystalline phases in the samples. Raman spectroscopy was performed using a Horiba Evolution system with a 532 nm laser wavelength. A 600 mm/gr diffraction grating and a 100x lens focused the laser. The acquisition time was set to 45 seconds with three accumulations, and a 25% filter was used. The spectral range measured was from 100 to 1200 cm^{-1}.

Optical transmittance measurements were conducted using a UV-Vis Evolution 220 spectrometer (Thermo Scientific), which covers wavelengths from 190 nm to 1100 nm. Contact angle measurements were performed using a Ramé-Hard Model 500 goniometer, with deionized water and diiodomethane as test liquids. Film thickness was measured with a KLA Tencor P7 profilometer. The film morphology was examined using a Tescan Vega 3 scanning electron microscope (SEM) operated at 5 kV.

2.3 Photoelectrochemistry measurements

Photoelectrochemical (PEC) measurements were conducted using a Metrohm AUTOLAB PGSTAT 302N potentiostat with a frequency response analysis (FRA) module. A standard three-electrode setup was employed, consisting of an Ag/AgCl (saturated KCl) reference electrode, a platinum wire as the

counter electrode, and the WO_x-based films (exposed area: 0.9 cm^2) as the working electrode. The experiments were carried out in a 0.5 M Na_2SO_4 cell within a quartz-window PEC aqueous electrolyte. The electrolyte was freshly replaced before each measurement for each sample.

Electrochemical impedance spectroscopy (EIS) was performed at open circuit potential (OCP) and under polarization at 0.36 V vs. Ag/AgCl, a potential chosen based on photocurrent density measurements under illumination. Measurements were taken before and after cyclic voltammetry to evaluate potential changes in interfacial properties. EIS spectra were recorded over a frequency range from 10^5 Hz to 0.1 Hz with a sinusoidal perturbation of 0.1 Vrms.

Mott–Schottky plots were obtained at a fixed frequency of 1000 Hz to estimate the flat-band potential and donor density, all conducted in dark conditions.

Cyclic voltammetry (CV) was performed both in the dark and under illumination, covering a potential range from –0.4 to +1.0 V vs. Ag/AgCl, at a scan rate of 25 $mV \cdot s^{-1}$. Illumination was provided by a solar simulator (ABET Technologies, model 10500), equipped with a 150 W DC xenon lamp and an AM 1.5G filter. The simulator was positioned 15 cm away from the PEC cell. The same simulator was used to determine the potential that yields maximum photoresponse, guiding the selection of polarization potential during EIS measurements.

3. Results and Discussion

3.1. Structure, morphology, and composition.

The target voltage was continuously monitored during the 60-minute deposition to assess how the oxygen flow ramp influences plasma behavior and the condition of the target surface (**Figure 2**). For tungsten, voltages below approximately 450 V typically indicate the metallic sputtering mode, where the target surface remains mostly metallic and erosion rates are high. In contrast, voltages near 510 V correspond to the compound sputtering mode, characterized by a fully oxidized target surface and a reactive plasma state [36].

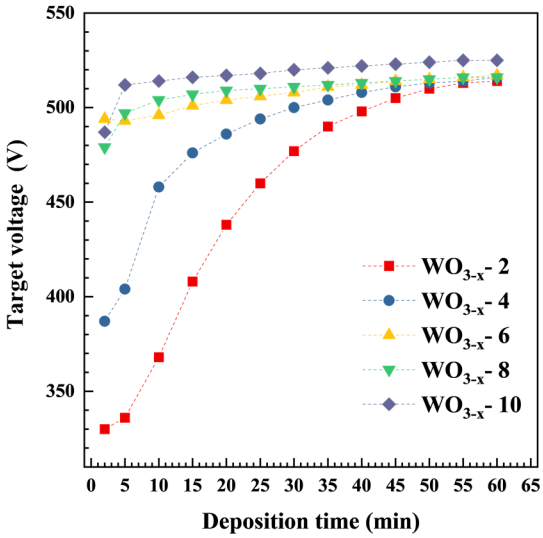

Figure 2 - Target voltage evolution during WO_{3-x} thin film deposition by DC reactive magnetron sputtering.

Samples with lower initial O_2 flows (WO_{3-x}-2 and WO_{3-x}-4) showed a slow increase in target voltage, taking longer to reach the compound regime. This indicates slower target poisoning, characterized by gradual surface oxidation, resulting in higher deposition rates initially.

On the other hand, higher initial O_2 flows (WO_{3-x}-6, WO_{3-x}-8, and WO_{3-x}-10) reached the compound regime quickly, suggesting the target was already partly oxidized from the start. This early stabilization encourages a more consistent film stoichiometry, although it generally produces lower deposition rates than the metallic mode.

Overall, the oxygen flow ramp profile controls the transition between metallic and compound sputtering modes, directly affecting the deposition rate, the final stoichiometry, and the electronic properties of the WO_{3-x} thin films.

The thickness of the WO_{3-x} thin films was measured using mechanical profilometry. The results showed an inverse relationship between film thickness and the oxygen flow rate during deposition. The WO_{3-x}–2 sample (2 sccm) had the greatest average thickness (1157 ± 50 nm), while WO_{3-x}–10 (10 sccm) had the lowest (536 ± 40 nm), as seen in **Figure 3**. The thickness measurements were taken three times for each sample, with error bars indicating the measurement uncertainty. This gradual decrease in thickness is due to the transition to the compound regime during reactive sputtering, where target poisoning by oxygen reduces the deposition rate because of the formation of an insulating oxide layer on the cathode surface. Similar behavior was reported by Olejníček et al. (2022), who observed a decrease in thickness with increasing oxygen flow because sputtering is suppressed under highly oxidizing conditions [37].

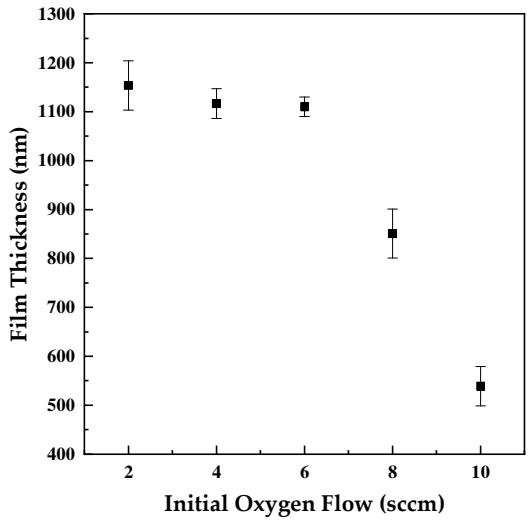

Figure 3 - Thickness of WO_{3-x} thin films as a function of initial oxygen flow during deposition

Figure 4 presents cross-sectional SEM images of all WO_{3-x} films. The thicknesses observed from these images are consistent with the profilometry data. Films deposited with the lowest initial oxygen flows, specifically WO_{3-x}-2 and WO_{3-x}-4, exhibit a distinct bilayer structure composed of a dense metallic base, measuring 183 nm and 115 nm thick, respectively, topped by a significantly thicker oxide overlayer. This stratification occurs because deposition begins under oxygen-deficient conditions that favor the growth of

metallic tungsten. As the oxygen flow increases and the target voltage stabilizes near 510 V, the plasma transitions to the compound sputtering regime, resulting in the formation of a WO_{3-x} layer on top.

The thicker metallic sublayer in WO_{3-x}-2 compared to WO_{3-x}-4 reflects the longer duration the target remained in metallic mode; the target voltage required several extra minutes to reach the 510 V threshold, allowing more W^0 to accumulate before complete target poisoning. In contrast, films grown with steeper oxygen ramps of six sccm or higher (WO_{3-x}-6, WO_{3-x}-8, and WO_{3-x}-10) entered the compound regime more quickly and developed a single-phase, compositionally uniform, and dense microstructure throughout their thickness, without the bilayer morphology seen in the other samples.

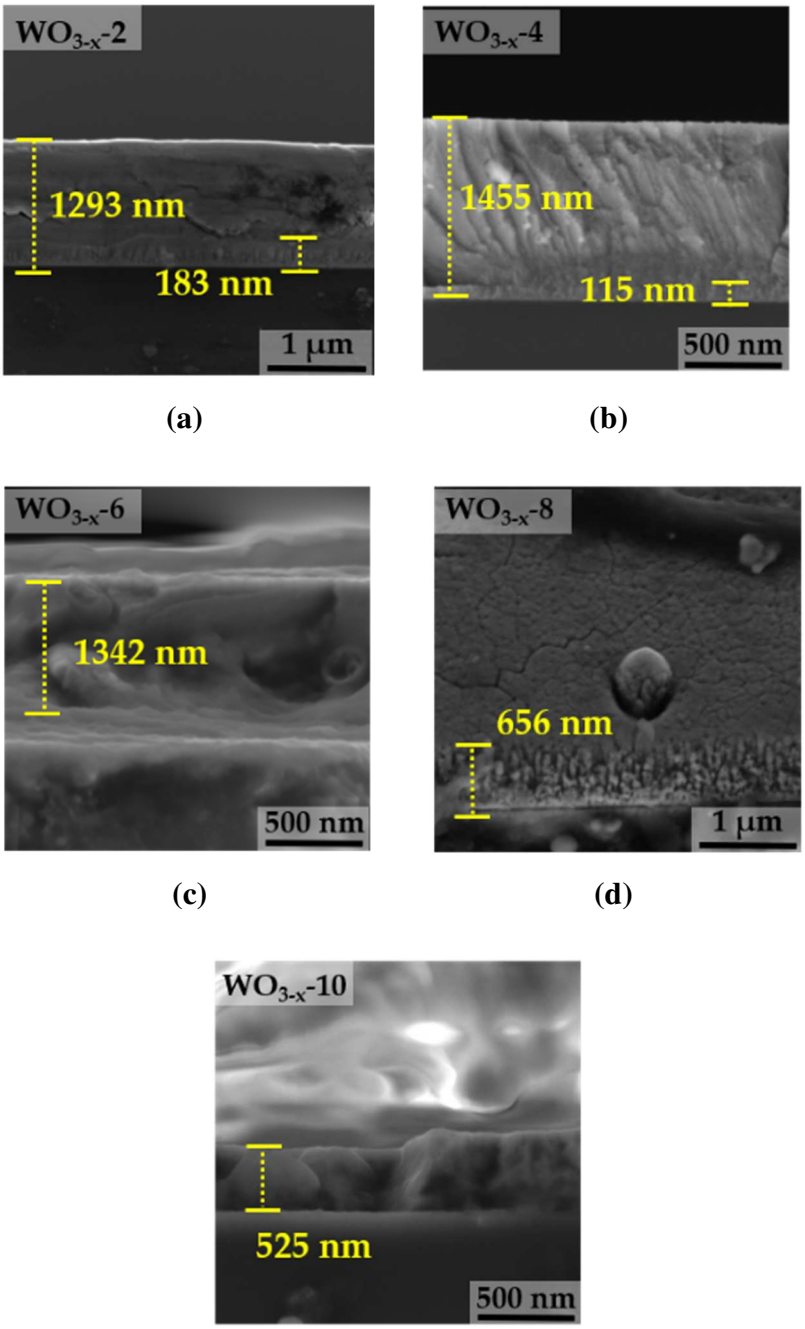

(e)

Figure 4 - Cross-sectional SEM images and corresponding thickness measurements of WO_{3-x} films deposited under progressively higher initial oxygen-flow ramps: (a) WO3-$_x$-2, (b) WO3-$_x$-4, (c) WO3-$_x$-6, (d) WO3-$_x$-8, and (e) WO3-$_x$-10.

Static contact-angle measurements with polar (water) and apolar (diiodomethane) liquids provided information on the surface wettability of WO_{3-x} thin films; the results are presented in **Table 1** and **Figure 5**. All samples exhibited hydrophilic behaviour, as confirmed by water contact angles below 40°, in agreement with previous studies [38,39]. Sample WO_{3-x}-8 showed the lowest angle (15.3°) and the highest total surface free energy (76.45 mJ m^{-2}); similarly high values were recorded for WO_{3-x}-6 (74.32 mJ m^{-2}) and WO_{3-x}-4 (75.64 mJ m^{-2}). These more energetic surfaces, enriched in polar components, favour both the adsorption of reactive species and the separation and extraction of charge carriers during photoelectrochemical operation. In contrast, WO_{3-x}-10 exhibited the largest contact angle (39.7°) and the lowest total surface free energy (65.27 mJ m^{-2}), whereas WO_{3-x}-2 displayed 34.9° and 69.47 mJ m^{-2}, respectively, indicating relatively more apolar surfaces compared with the films obtained under intermediate oxygen ramps.

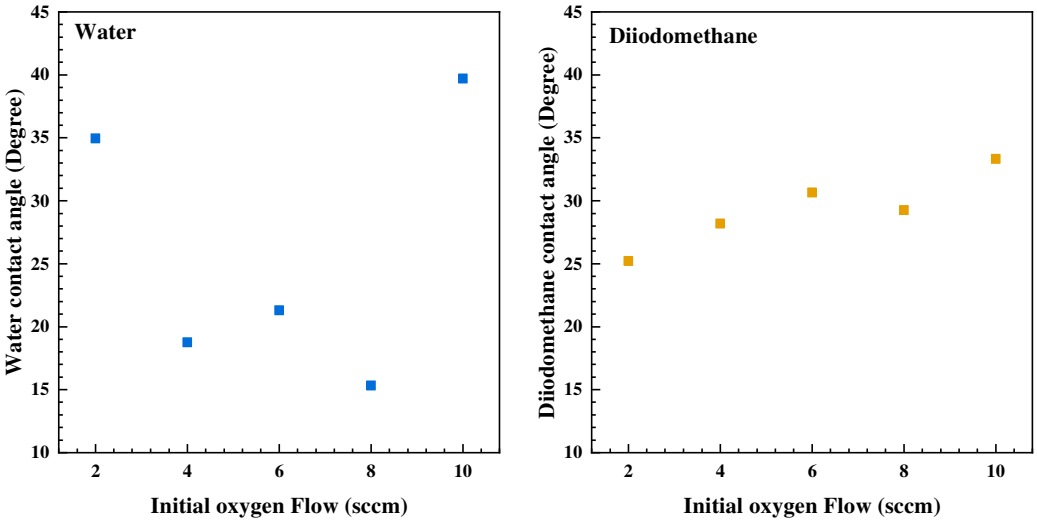

(a) **(b)**

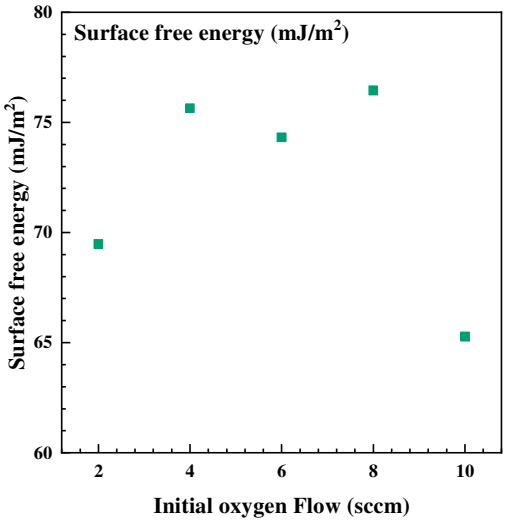

(c)

Figure 5 - Influence of the initial oxygen flow on (a) the contact angles of water, (b) the contact angles of diiodomethane, and (c) the total surface free energy of WO_{3-x} films.

Table 1 - Static contact angles and surface-free-energy components of WO_{3-x} films

Sample	Water (Angle)	Diiodomethane (Angle)	Polar Component (mJ/m^2)	Dispersive Component (mJ/m^2)	Surface Free Energy (mJ/m^2)
WO_{3-x} - 2	34.95 ± 0.01	25.21 ± 0.04	23.40 ± 0.01	46.08 ± 0.01	69.47 ± 0.01
WO_{3-x} - 4	18.76 ± 0.01	28.19 ± 0.01	30.69 ± 0.01	44.95 ± 0.01	75.64 ± 0.01
WO_{3-x} - 6	21.31 ± 0.01	30.67 ± 0.01	30.38 ± 0.01	43.94 ± 0.01	74.32 ± 0.01
WO_{3-x} - 8	15.33 ± 0.01	29.26 ± 0.01	31.92 ± 0.01	44.53 ± 0.01	76.45± 0.01
WO_{3-x} - 10	39.71 ± 0.01	33.33 ± 0.01	22.48 ± 0.01	42.79 ± 0.01	65.27 ± 0.01

3.2. Crystallographic and Vibrational Analysis

The X-ray diffraction (XRD) analysis was performed to identify the crystalline phases present in the WO_{3-x} films. The patterns were refined using the Le Bail method [40,41], a whole-pattern fitting procedure that allows extraction of unit cell parameters without requiring knowledge of atomic positions. The refinements were implemented in the HighScore Plus software package [35], which enables reliable deconvolution of overlapping peaks and precise determination of lattice parameters.

The diffraction patterns (**Figure 6**) show that all samples exhibit exclusively the monoclinic γ-WO_3 phase ($P2_1/n$, space group 14; ICSD PDF 01-089-4476). The only additional peaks detected originate from the fluorine-doped tin oxide (FTO) substrate and are indicated with black dashed lines in the last diffractogram. No reflections from metallic tungsten or sub-stoichiometric tungsten oxides were observed, suggesting that even the film deposited under the lowest initial oxygen flow conditions is predominantly oxidized. This behavior is consistent with studies reported in the literature, which indicate that the monoclinic phase remains stable up to 400 °C in WO_3 nanoparticles, with phase transition to β-WO_3 only occurring at 500 °C [42,43].

The absence of metallic tungsten or sub-stoichiometric phases in the XRD patterns may result from the thermal treatment performed in ambient air to develop the crystalline phase. This process could

have led to the reoxidation of the samples, possibly diminishing the effect of the oxygen flow ramp applied during deposition. As a result, the gradual increase in oxygen flow during deposition might have been counteracted during post-deposition heat treatment, leading to the exclusive formation of the γ-WO_3 phase observed in the XRD data.

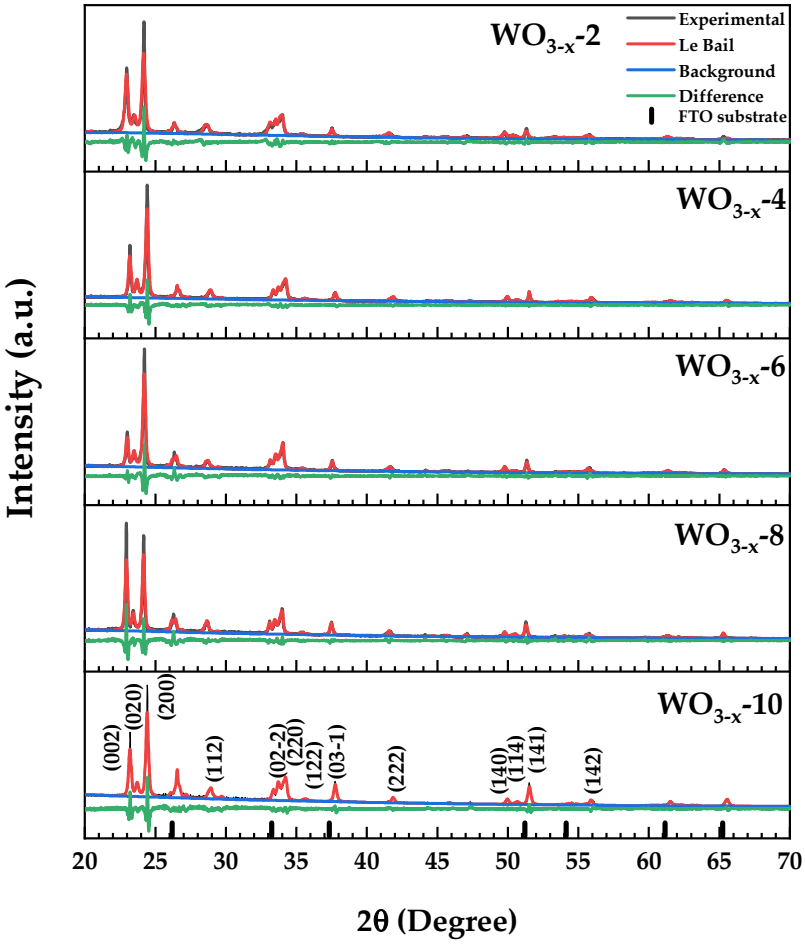

Figure 6 - X-ray diffraction patterns of WO_{3-x} films. For each sample, the experimental profile (black) is overlaid with the Le Bail refinement (red), the fitted background (blue), and the difference curve (green). Reflection indices correspond to monoclinic γ-WO_3 (ICDD PDF 01-089-4476); tick marks at the bottom indicate peaks from the FTO substrate.

Refinement results are summarized in **Table 2**. Among the films, WO_{3-x}–2 exhibits the largest unit cell volume, which progressively contracts with increasing oxygen flow, stabilizing at approximately 424.5 Å³ for flows above 4 sccm. This contraction is attributed to the reduced concentration of oxygen vacancies as more oxygen is incorporated into the lattice, leading to restoration of W–O bonds and shortening of lattice parameters [43]. Similar structural relaxation with decreasing vacancy concentration has also been reported for WO_{3-x} films deposited via sputtering under different oxygen regimes [43].

Furthermore, the microstrain (ε), which reflects lattice distortions due to defects or stress, decreases from 0.60% in WO_{3-x}–2 to 0.43% in WO_{3-x}–8, corroborating the progressive lattice relaxation as the film approaches stoichiometry. A slight increase in ε to 0.46% for WO_{3-x}–10 may be related to residual stresses induced by lower deposition rates and enhanced ion bombardment in highly oxidizing plasma environments, as also noted by Hrubantova et al. (2022) in similar sputtering conditions [43].

The average crystallite size also follows a trend consistent with reduced disorder and improved crystalline quality under increased oxygen flow. It increases from 31 nm in WO_{3-x}–2 to a maximum of 43.7 nm in WO_{3-x}–8. This observation aligns with previous findings where enhanced oxidizing atmospheres during sputtering promoted grain growth and crystallinity [43].

In conclusion, the distinct structural parameters observed for WO_{3-x}–2 suggest that despite the reoxidation treatment undergone during thermal annealing, this sample may still retain some structural defects, particularly oxygen vacancies. These defects may have prevented full lattice relaxation, contributing to the observed differences in the XRD results.

Table 2 - Refined structural parameters of monoclinic γ-WO_3 thin films. Listed are the lattice parameters *a*, *b*, *c*, *β* angle, and unit-cell volume of the monoclinic unit cell, microstrain, crystallite size, and the goodness-of-fit indicators χ^2, R_{exp} and R_{wp} obtained from Le Bail refinements of the X-ray diffraction data.

Sample	α (Å)	b (Å)	c (Å)	β (deg)	Unit cell vol (Å^3)	Microstrain (%)	Crystallite size (nm)	χ^2	R_{exp}	R_{wp}
WO_{3-x} - 2	7.3570(1)	7.5520(7)	7.7390(1)	90.648(9)	429.95(4)	0.600	31.5(5)	4.255	5.5128	11.3729
WO_{3-x} - 4	7.3130(6)	7.5276(5)	7.6926(6)	90.513(6)	423.46(6)	0.480	38.16(2)	3.001	5.7150	9.9112
WO_{3-x} - 6	7.3190(3)	7.5367(3)	7.6959(4)	90.510(6)	424.50(3)	0.476	39.61(2)	3.213	5.7819	10.3656
WO_{3-x} - 8	7.3205(9)	7.5389(6)	7.700(1)	90.505(7)	424.94(6)	0.433	43.7(1)	4.140	5.8721	11.9481
WO_{3-x} - 10	7.3173(7)	7.533(4)	7.6984(5)	90.547(7)	424.33(5)	0.461	40.49(5)	2.446	6.2945	9.8451

As a complementary technique to X-ray diffraction, Raman spectroscopy was employed to investigate the vibrational modes of the WO_{3-x} films and to support the identification of the crystalline phases. The spectra obtained (**Figure 7**) exhibit the typical vibrational fingerprint of monoclinic γ-WO_3, with no evidence of secondary or amorphous phases [44].

Raman spectroscopy revealed the main vibrational modes of the monoclinic γ-WO_3 phase at approximately 132, 182, 271, 325, 714, and 806 cm^{-1}. These bands are attributed to lattice vibrations (≤ 200 cm^{-1}), O–W–O bending (~270–330 cm^{-1}), and W–O stretching modes (~712–810 cm^{-1}), consistent with the monoclinic γ-phase of WO_3. The assignments are corroborated by previous studies, which associate the bands at ~270 and 326 cm^{-1} with O–W–O bending modes and the bands at ~712 and 806 cm^{-1} with asymmetric and terminal W=O stretching modes, respectively [37,43,45].

The broadening of the Raman peaks in the lower frequency region for WO_{3-x}-2 and WO_{3-x}-4 suggests increased structural disorder and a higher concentration of oxygen vacancies. The progressive blue-shift of the 714 cm^{-1} band and the intensity rise of the 806 cm^{-1} band with increasing O_2 flow indicate a local oxidation of tungsten sites, consistent with previous observations [45,46]. This behavior corroborates the XRD results for the WO_{3-x}-2 sample, which also showed evidence of structural defects and oxygen vacancy formation. These results align with the idea that WO_{3-x}-2, despite the reoxidation treatment, may still retain some oxygen vacancies, contributing to the observed spectral shifts.

The persistence of all major vibrational modes across the entire series of samples, regardless of the oxygen flow conditions, reinforces the structural findings from XRD and confirms the dominance of the monoclinic γ-WO_3 phase throughout the set.

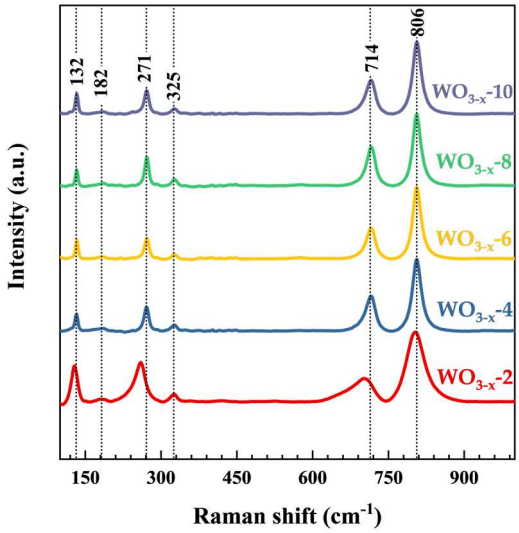

Figure 7 - Raman spectra (λ exc = 532 nm) of WO_{3-x} films. The dashed lines mark the main vibrational modes of monoclinic γ-WO_3.

3.3. Optical Properties

UV-Vis transmittance spectroscopy is a widely employed technique for the optical characterization of semiconductor thin films, as it enables the evaluation of electromagnetic radiation absorption as a function of the energy of incident photons. Through analysis of the transmittance spectra, it is possible to estimate fundamental properties such as the optical bandgap energy (Eg), the presence of intermediate states, and the structural quality of the material. Transmittance is sensitive to variations in thickness, morphology, and stoichiometry, making it an essential tool for the assessment of materials intended for optoelectronic devices, solar cells, and photoelectrodes.

In this study, the spectra obtained for WO_{3-x} thin films revealed typical behavior of semiconductors with an indirect bandgap, exhibiting significant transmittance in the visible range and an absorption edge that shifts toward longer wavelengths as the oxygen flow during deposition decreases.

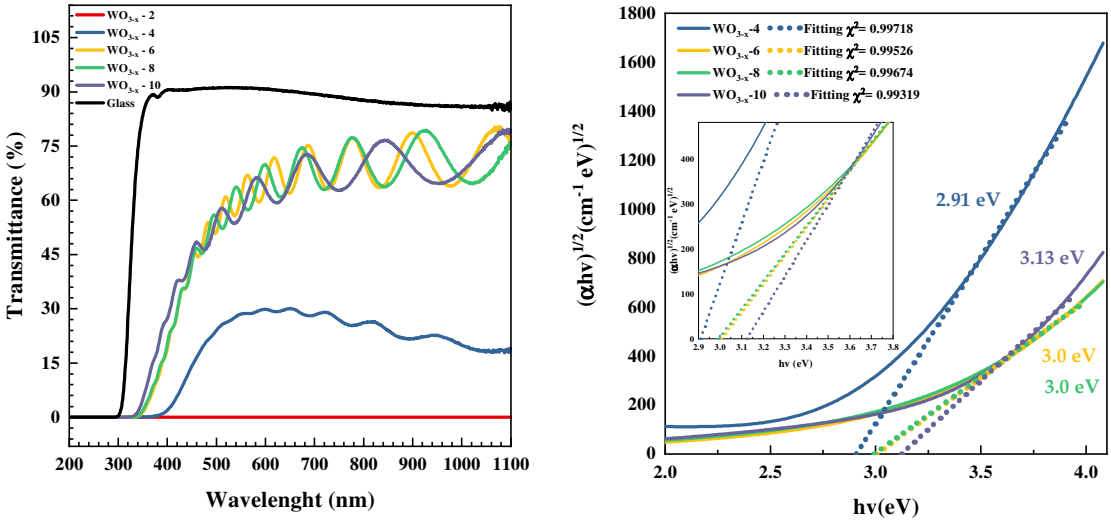

(a) (b)

Figure 8 - (a) UV–Vis–NIR transmittance spectra (200–1100 nm) of WO_{3-x} films grown with initial oxygen flows of 2, 4, 6, 8 and 10 sccm. (b) Tauc plots for the translucent samples; dotted lines are the linear fits used to determine the indirect optical band gap.

The transmittance spectra demonstrate a strong influence of the initial O_2 flow on the optical transparency of the films (**Figure 8(a)**). The sample WO_{3-x}-2 is practically opaque throughout the entire spectral range, due to its high thickness (~ 1.3 µm) and dark coloration. For oxygen flows between 4 and 10 sccm, the visible transmittance reaches 70–75%, displaying well-defined interference fringes that confirm good thickness uniformity and low extinction coefficients.

The optical bandgap energy (Eg) was determined using the Tauc method, which is widely used for the analysis of semiconductor materials [47]. This method relates the absorption coefficient (α) to the photon energy (hv) through the following **Eq.2**:

$$(\alpha h\nu)^{1/n}=A(h\nu-E_g), \qquad \textbf{Eq.2}$$

where A is a constant, Eg represents the bandgap energy, and the exponent n depends on the type of electronic transition involved [47]. For indirect transitions, as in the case of WO_{3-x}, the exponent n is equal to 0.5. This selection is supported by the structural characteristics of tungsten oxide and is confirmed in the recent literature [31,37,48,49]. Thus, the plot was constructed by plotting $(\alpha h\nu)^{0.5}$ versus hv, and the Eg value was obtained by extrapolating the linear portion of the curve to the energy axis.

The analysis (**Figure 8(b)**) indicates that the indirect optical bandgap increases with stoichiometry: from 2.91 eV in WO_{3-x}-4 to 3.13 eV in WO_{3-x}-10, passing through 3.00 eV in WO_{3-x}-6 and WO_{3-x}-8. One hypothesis is that this bandgap widening is associated with a gradual decrease in the concentration of oxygen vacancies and W^{5+} cations, whose presence in WO_{3-x}-4 reduces the band separation by introducing shallow donor levels. As the target becomes rapidly poisoned (flows ≥ 6 sccm), the W^{6+} content increases and donor states are suppressed, shifting the absorption edge toward higher energies.

The coincidence between the gap values (~ 3.0–3.1 eV) and the region of maximum surface free energy (WO_{3-x}-6 and WO_{3-x}-8) suggests that an intermediate concentration of vacancies simultaneously

optimizes transparency, surface activity, and photoelectrochemical performance. WO_{3-x}-10, although more transparent and exhibiting a wider bandgap, presents lower surface polarity and therefore a reduced electrochemically active area.

Previous studies support the interpretation of these results. CHANANONNAWATHORN et al. (2012) demonstrated that reducing the oxygen flow during the sputtering deposition of WO_3 leads to a decrease in the bandgap energy, due to the increased concentration of vacancies and greater structural disorder [31]. HRUBANOVA et al. (2022) reported variations in Eg values ranging from 2.6 to 3.1 eV, depending on the stoichiometry and thermal treatment applied to the films [48].

Therefore, the transmittance results demonstrate that controlling the oxygen flow during film deposition is a crucial factor in engineering the band structure of WO3-x films, allowing for the tuning of their optical properties as desired, in agreement with findings reported in the literature.

3.4. Photoelectrochemistry Properties

Electrochemical impedance spectroscopy (EIS) is a powerful technique used to probe interfacial charge transfer phenomena and the electrical behavior of electrochemical systems over a range of frequencies. In the context of photoelectrochemical (PEC) water splitting, EIS enables the investigation of key parameters, including solution resistance (R_s), charge transfer resistance (R_1), and diffusion or recombination-related resistance in the bulk or interface (R_p). These parameters, extracted via fitting with equivalent circuits, provide insight into the semiconductor/electrolyte interface dynamics, the effectiveness of charge separation, and the degree of disorder or defectiveness within the electrode material [50].

In this study, EIS measurements were performed under open-circuit potential (OCP) and under anodic polarization at +0.36 V vs. Ag/AgCl, both before and after cyclic voltammetry under simulated solar illumination. The Nyquist plots obtained are presented in **Figure 9**, and the equivalent circuit used for fitting is shown in **Figure 10**. This model comprises two time constants: one associated with the electrode/electrolyte interface ($R_1||CPE_1$) and another with transport or accumulation within the film ($R_p||CPE_2$).

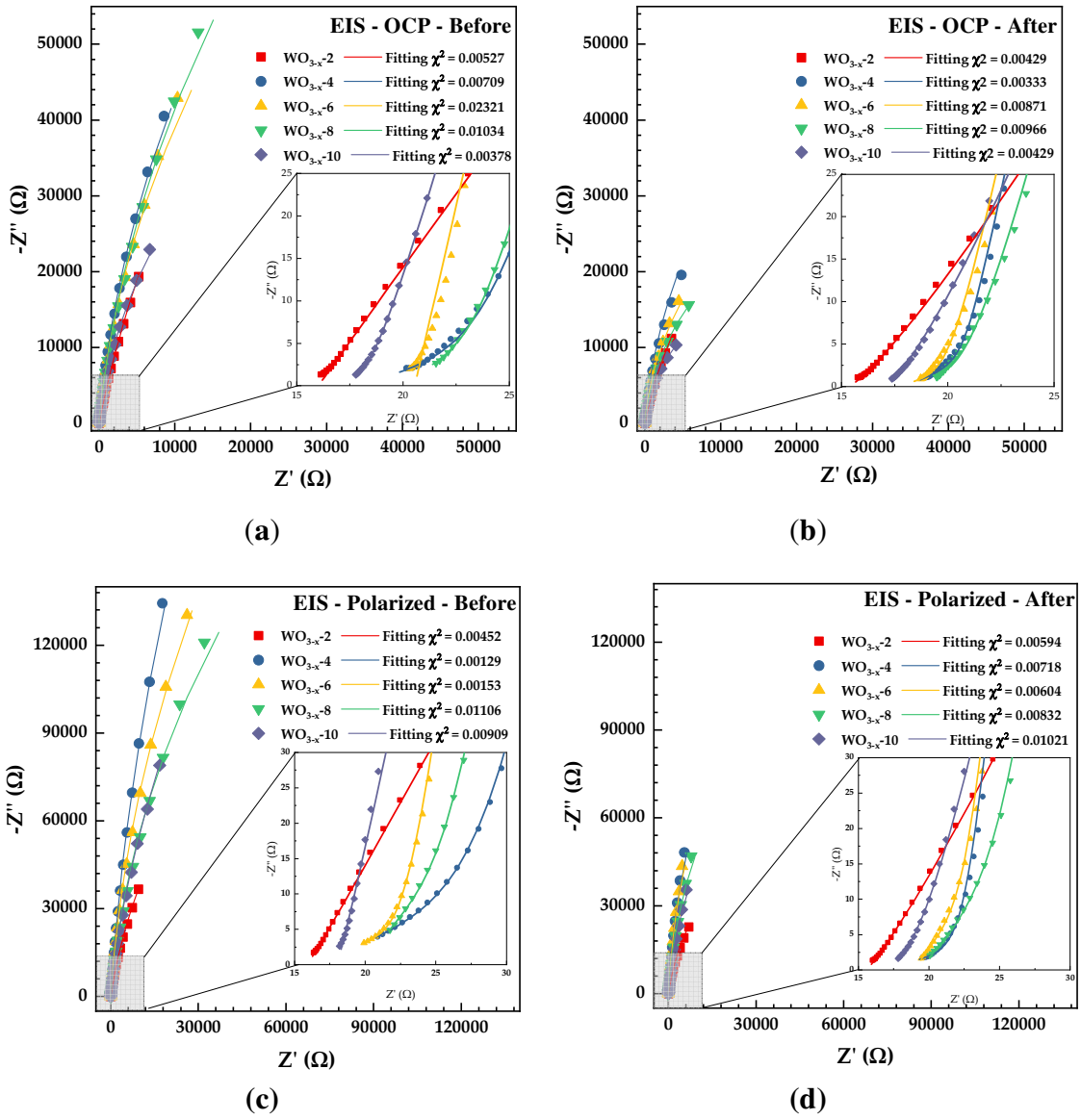

Figure 9 - Nyquist plots obtained from electrochemical impedance spectroscopy (EIS) for the WO_{3-x} electrodes under four experimental conditions: (a) open-circuit potential (OCP) before photoelectrochemical testing, (b) OCP after illumination, (c) under anodic polarisation before illumination, and (d) under the same polarisation after illumination.

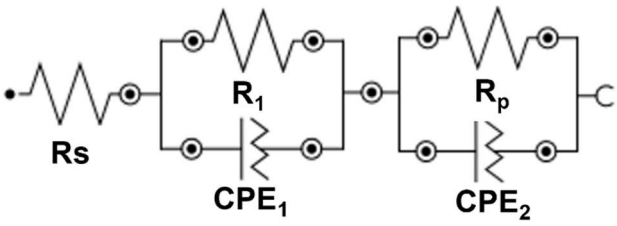

Figure 10 - Equivalent electrical circuit employed to fit the EIS data.

The fitting parameters are summarized in **Table 3**. The solution resistance R_s remained almost constant across all samples (15–21 Ω), indicating that the impedance differences observed are mainly due

to interfacial phenomena. The charge transfer resistance R_1, measured under OCP conditions, showed a clear trend among the samples. Initially, the resistances were around 50,000 Ω, but after cyclic voltammetry and exposure to simulated solar light, this resistance decreased to approximately 20,000 Ω. This decline suggests that the material exhibited photoactivity, resulting in better charge separation at the electrode/electrolyte interface under illumination.

A similar trend was seen for R_p. In the OCP condition, R_p was generally higher across all samples, indicating the material's inherent resistance to charge transport and recombination. After light exposure, R_p dropped notably, especially in WO_{3-x}–4 and WO_{3-x}–6, indicating that light helped improve charge mobility in the films. The reduction in R_p after illumination suggests that photoinduced effects, such as passivation of shallow traps, improved charge separation, and increased capacitance of the electrical double layer, occurred.

Under polarization at +0.36 V, the semicircles shifted to higher frequencies while maintaining the resistance hierarchy. The samples showed higher R_1 and R_p values under polarized conditions compared to OCP. This is expected since polarization generally results in higher resistance due to increased ion build-up at the interface. After illumination, both R_1 and R_p decreased for all samples, with the most notable reductions seen in WO_{3-x}–6 and WO_{3-x}–8, experiencing about 40% decreases. This suggests that light-induced effects continue even under bias, improving interfacial charge transfer and supporting the material's performance in PEC applications.

Table 3 - Fitted electrochemical-impedance parameters for WO_{3-x} electrodes under different measurement conditions.

Sample	Condition	Rs (Ω)	R1 (Ω)	Y_{01} (μMho·s^n)	N_1	Rp (Ω)	Y_{02} (μMho·s^n)	N_2
WO_{3-x}-2	OCP Before	16.0	25.3	996.0	0.701	285000	73.7	0.878
	OCP After	15.3	18.7	6060	0.509	112000	124	0.878
	Polarized Before	15.9	66.8	487	0.688	356000	39.3	0.907
	Polarized After	15.6	29.7	1540	0.602	162000	61.0	0.909
WO_{3-x}-4	OCP Before	17.9	8.74	1410	0.472	307000	35.6	0.945
	OCP After	18.2	2.73	493	0.672	147000	74.7	0.951
	Polarized Before	16.7	15.8	352	0.522	189000	11.5	0.957
	Polarized After	17.1	6.35	930	0.483	563000	32.2	0.971
WO_{3-x}-6	OCP Before	20.5	94200	53.3	0.929	475000	81.0	0.967
	OCP After	17.8	2.79	2650	0.504	81700	87.9	0.946
	Polarized Before	16.2	6.89	96.7	0.623	975000	11.4	0.955
	Polarized After	19.0	3.64	279	0.777	546000	35.7	0.97
WO_{3-x}-8	OCP Before	20.0	3.76	276	0.683	318000	27.0	0.935
	OCP After	50.8	4.93	166000	0.00313	64500	86.3	0.939
	Polarized Before	20.2	4.99	49.3	0.834	645000	11.5	0.945
	Polarized After	19.2	6.89	521	0.669	352000	32.5	0.964
WO_{3-x}-10	OCP Before	15.6	3.65	3460	0.384	131000	60.8	0.928
	OCP After	17.1	399000	134	0.943	39000	3630	0.591
	Polarized Before	18.0	30600	73.9	0.857	843000	23.6	0.993
	Polarized After	16.7	297000	42.7	0.956	703000	14800	0.365

Cyclic voltammograms revealed significant differences in the electrochemical behavior of the films as a function of their oxygen content, as shown in **Erreur ! Source du renvoi introuvable.** Notably, the WO_{3-x}-2 and WO_{3-x}-4 samples exhibited an anodic peak around −0.1 V vs. Ag/AgCl, which was absent in the other samples. This peak, observed exclusively under dark conditions, was attributed to the oxidation of W^{5+} to W^{6+} species, a process favored by the higher density of oxygen vacancies in the films with lower oxygen content [50,51]. The presence of oxygen vacancies tends to stabilize reduced tungsten states (W^{5+}), which, upon oxidation during the forward scan, give rise to a characteristic anodic peak at negative potentials. This behavior is consistent with the literature, where the $W^{5+} \rightarrow W^{6+}$ oxidation process is reported to be predominant in sub-stoichiometric WO_3 films, particularly in neutral electrolytes that do not promote significant ionic intercalation [50,52].

In contrast, the WO_{3-x}-6, WO_{3-x}-8, and WO_{3-x}-10 samples, which contain higher oxygen concentrations, did not exhibit this anodic peak, indicating that the concentration of W^{5+} species is substantially lower or negligible in these compositions. In these cases, the electrochemical behavior was predominantly capacitive, with more stable and symmetric currents in both branches of the voltammetric curve. Under dark conditions, the current densities ranged from −0.035 to 0.0025 mA·cm^{-2}. Upon light irradiation, all samples exhibited a significant increase in current, with values ranging from −0.07 to 1.3 mA·cm^{-2}. This behavior is characteristic of the photoelectrochemical activation of WO_3 films, whose bandgap enables the generation of electron–hole pairs under illumination. The photocurrent response was particularly pronounced for the WO_{3-x}-8 sample, indicating higher efficiency in photogenerated charge separation and electronic transport [24,52]. Moreover, the absence of the anodic peak at −0.1 V under illumination further supports the hypothesis that this feature is exclusively associated with re-dox-active tungsten species stabilized under dark conditions.

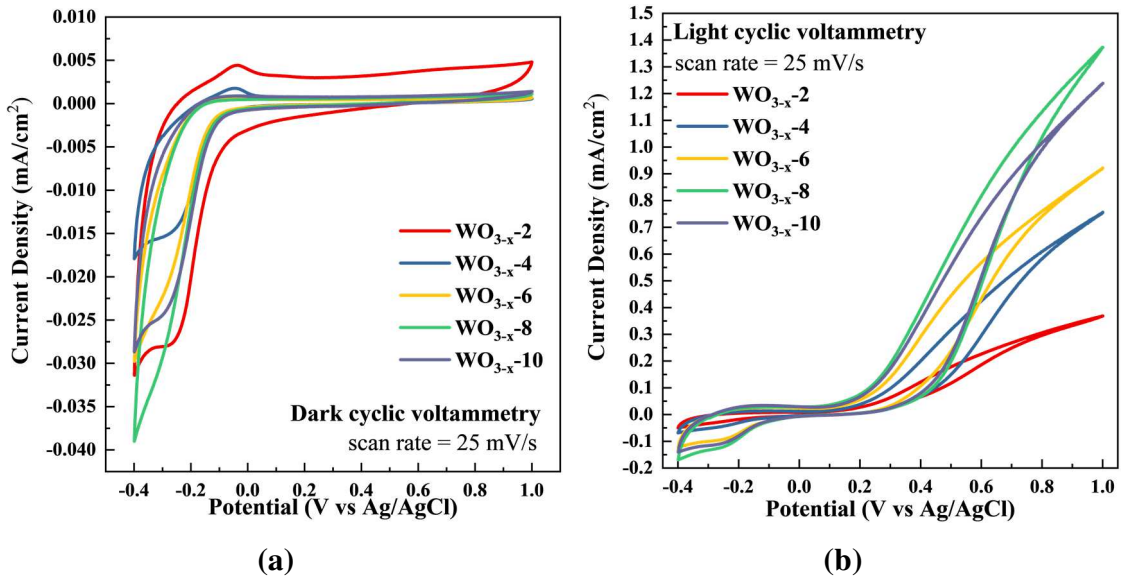

Figure 11 - Cyclic-voltammetry curves of WO_{3-x} electrodes at a scan rate of 25 mV s^{-1}. (a) Responses under dark conditions; (b) photo-assisted responses under AM 1.5G illumination (100 mW cm^{-2}).

The quantitative analysis of the electrochemical properties was performed based on specific capacitance (Cs), specific energy (Es), and specific power (Ps), as shown and summarized in **Table 4**.

The specific capacitance values varied among the samples according to the film composition. The WO_{3-x}-8 sample exhibited the highest specific capacitance (0.376 mF·cm^{-2}), followed by WO_{3-x}-10 and WO_{3-x}-2. The lowest value was recorded for WO_{3-x}-4 (0.188 mF·cm^{-2}), indicating that an increase in oxygen content does not necessarily lead to a proportional increase in capacitance. The WO_{3-x} -8 sample stood out with the highest values across all metrics, suggesting an optimal point in the concentration of oxygen vacancies. This behavior supports the idea that there is an ideal balance between the density of oxygen vacancies and structural integrity to maximize electrochemical performance [53,54].

Table 4 - Photo-enhanced electrochemical performance metrics of WO_{3-x} electrodes extracted from cyclic-voltammetry data.

Sample	Specific Capacitance (mF/cm²)	Specific Power (W/cm²)	Specific Energy (Wh/cm²)
WO_{3-x} – 2_dark	0.29	8.0E-06	0.42
WO_{3-x} – 2_light	11.0	3.8E-04	32.4
WO_{3-x} – 4_dark	0.18	5.3E-06	0.22
WO_{3-x} – 4_light	19.8	5.5E-04	60.4
WO_{3-x} – 6_dark	0.28	7.9E-06	0.36
WO_{3-x} – 6_light	28.9	8.1E-04	86.7
WO_{3-x} – 8_dark	0.37	9.7E-06	0.49
WO_{3-x} – 8_light	39.3	1.0E-03	110
WO_{3-x} – 10_dark	0.30	8.5E-06	0.40
WO_{3-x} – 10_light	36.0	1.0E-03	109

The specific energy exhibited a similar trend: WO_{3-x}-8 again stood out with the highest value (0.49 Wh·cm^{-2}), while WO_{3-x}-4 showed the poorest energy performance (0.22 Wh·cm^{-2}). This superior performance of the WO_{3-x}-8 sample can be attributed to its optimized oxygen vacancy structure, which is sufficient to promote surface redox processes without compromising structural stability, unlike samples with either excess or deficiency of oxygen. Similarly, the specific power, which depends on the discharge time and the charge transport rate, also peaked for WO_{3-x}-8 (1.05×10^{-5} W·cm^{-2}), further corroborating the excellent overall performance of this composition. These results suggest that there is an optimal concentration of oxygen vacancies that simultaneously favors charge storage mechanisms and enhances electrochemical response speed.

Oxygen vacancies are critical structural defects that drastically influence the electronic and electrochemical properties of transition metal oxides. In the case of WO_3, these vacancies introduce intermediate electronic states (donor defects) that facilitate electronic conduction and the formation of W^{5+} species [51]. However, an excessive presence of vacancies can compromise material stability and lead to the degradation of capacitive performance, as observed for the WO_{3-x}-4 sample. Conversely, in the more oxygen-rich samples, the absence of active redox species reduces faradaic storage, resulting in predominantly non-faradaic (purely capacitive) behavior.

Thus, a nonlinear relationship is observed between oxygen content and electrochemical performance. The balance between a sufficient density of oxygen vacancies, enabling surface redox reactions, and an ordered structure that maintains electrochemical stability appears to be achieved in the

WO3-x-8 sample, which exhibits the best results in terms of capacitance, energy, and power, as well as the highest efficiency under illumination.

Mott–Schottky (MS) analysis is a classical technique widely employed to evaluate the semiconductor–electrolyte interface properties in photoelectrochemical (PEC) systems. By measuring the interfacial capacitance (C) as a function of the applied potential (V), it is possible to extract two key parameters: the flat-band potential (V_{fb}), which indicates the alignment of energy bands with respect to the redox levels of the electrolyte; and the donor density (N_D), which provides insight into the concentration of free carriers within the semiconductor. In an ideal n-type semiconductor, a linear region in the $1/C^2$ vs. V plot is expected, where the slope is inversely proportional to N_D. In the context of PEC water splitting, these parameters are critical for assessing band energetics and carrier transport behavior under operational conditions.

The $1/C^2$ vs. V curves obtained for WO_{3-x} films deposited under different initial O_2 flow ramps are shown in **Figure 12**. The corresponding values of V_{fb} and N_D, extracted from the linear region of the plots, are summarized in **Table 5**. A parabolic trend was observed in both parameters, highlighting a strong dependence on oxygen stoichiometry.

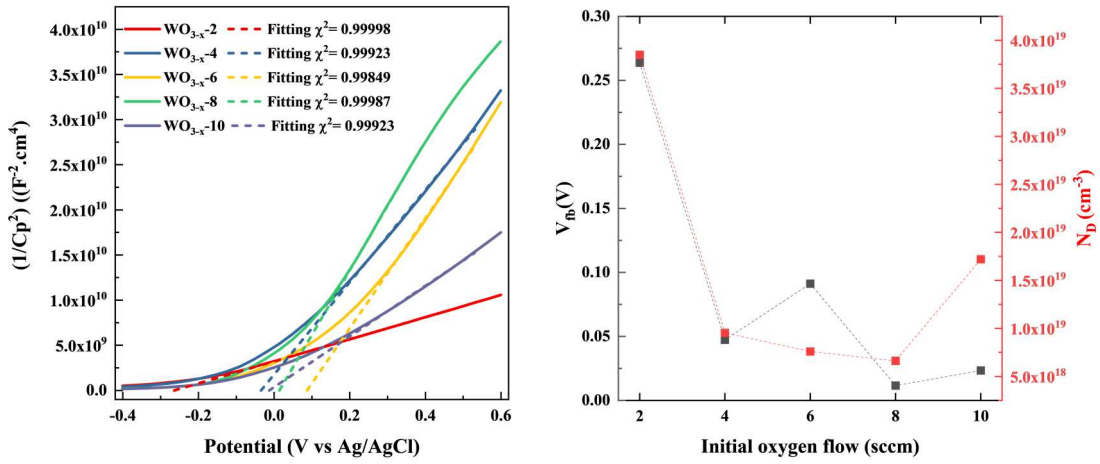

Figure 12 - (a) Mott–Schottky plots for WO_{3-x} electrodes; the dashed lines are linear fits used to extract the donor density N_D and flat-band potential V_{fb}. (b) Evolution of V_{fb} (black squares, left axis) and N_D (red circles, right axis) as a function of the initial oxygen-flow ramp employed during film deposition.

Table 5 - Flat-band potential V_{fb} and donor density N_D obtained from Mott–Schottky analysis of WO_{3-x} films as a function of the initial oxygen-flow ramp during deposition

Sample	V_{fb} (V)	N_D (cm^{-3})
WO_{3-x} – 2	0.2637	3.85×10^{19}
WO_{3-x} – 4	0.0472	9.53×10^{18}
WO_{3-x} – 6	0.0911	7.59×10^{18}
WO_{3-x} – 8	0.0116	6.61×10^{18}
WO_{3-x} – 10	0.0233	1.72×10^{19}

The sample WO_{3-x}-2, prepared with minimal oxygen flow, exhibited the most positive flat-band potential (V_{fb} = 0.2637 V) and the highest donor density ($N_D = 3.85 \times 10^{19}$ cm^{-3}). These values indicate a degenerate doping regime, likely due to a high concentration of oxygen vacancies acting as shallow donors.

However, this excessive donor concentration can also lead to significant recombination, as evidenced by the poor photocurrent and high charge transfer resistance seen in previous electrochemical impedance spectroscopy (EIS) results.

As the oxygen flow increased to 4 and 6 sccm, both V_{fb} and N_D decreased markedly. In WO_{3-x}-4, the flat-band potential dropped to 0.0473 V and N_D to 9.53×10^{18} cm^{-3}. In WO_{3-x} -6, V_{fb} reached 0.0912 V and N_D dropped further to 7.59×10^{18} cm^{-3}. This decrease suggests improved band alignment and a more favorable depletion layer for photoinduced charge separation. Notably, these samples also presented lower R_1 values in EIS and enhanced photocurrent response in cyclic voltammetry, demonstrating a coherent correlation across techniques.

WO_{3-x}-8 exhibited the most negative flat-band potential (V_{fb} = 0.0116 V), alongside a moderate donor density of 6.61×10^{18} cm^{-3}. The strong negative shift in V_{fb} implies an enhanced band bending, favoring the migration of holes toward the electrolyte. This sample also exhibited the highest interfacial capacitance (CPE_1) and the lowest charge transfer resistance under light (R_1 ~ 2.7 kΩ), reinforcing the hypothesis that PEC performance is maximized when the carrier density is high enough to ensure conductivity, but not so high as to induce recombination.

At the highest oxygen flow (WO_{3-x} -10), V_{fb} increased slightly (0.0234 V), while N_D rose to 1.72×10^{19} cm^{-3}. This partial recovery in carrier density might result from a reintroduction of sub-stoichiometric defects. Nevertheless, the structural and optical characterizations indicated lower crystallinity and reduced visible light absorption in this sample, which, together with its relatively high R_p value in EIS, compromises its overall PEC efficiency.

Importantly, the MS results are consistent with trends observed in the optical bandgap and surface wettability. The samples with intermediate oxygen flow (WO_{3-x}-6 and WO_{3-x}-8) exhibited lower band gaps (~3.0 eV), higher polar surface free energy, and improved contact angle performance, indicating a synergistic effect among structural order, surface chemistry, and electronic properties.

In summary, Mott–Schottky analysis confirms that the initial oxygen flow modulates the electronic structure of WO_{3-x} films, primarily by controlling the density of donor-like oxygen vacancies and shifting the flat-band potential. Optimal PEC performance is achieved in a narrow window (6–8 sccm), where charge carrier density, interfacial energetics, and structural properties are all favorably balanced.

The combined photoelectrochemical analyses reveal that the performance of WO_{3-x} thin films is strongly governed by the interplay between oxygen vacancy concentration and the resulting modifications in interfacial energetics, charge transport, and redox activity.

4. Conclusions

This study demonstrated that the application of an oxygen ramp during the deposition of WO_{3-x} thin films by magnetron sputtering, aimed at forming an oxygen gradient along the film thickness, directly influences their structural, optical, and photoelectrochemical properties. It was observed that increasing the initial oxygen flow reduced the deposition rate and, consequently, the final thickness of the films, as evidenced by mechanical profilometry. These results were corroborated by SEM images, which showed the progressive decrease in thickness and revealed a bilayer morphology for the WO_{3-x}–2 and WO_{3-x}–4 samples, while the others exhibited compact and dense morphologies.

XRD and Raman analyses confirmed the formation of the monoclinic phase in all samples, with no evidence of metallic tungsten or significant oxygen vacancies. This behavior may be attributed to the post-deposition thermal treatment in ambient atmosphere (450 °C for 2 h), which likely promoted film reoxidation and reduced the gradient initially induced during deposition. Nevertheless, the WO_{3-x}–2 and WO_{3-x}–4 samples exhibited variations in the structural parameters obtained from Le Bail refinement and shifts in Raman peaks, indicating a greater degree of structural disorder associated with oxygen vacancies. Photoelectrochemical measurements supported these findings, revealing anodic peaks corresponding to $W^{5+} \rightarrow W^{6+}$ oxidation in WO_{3-x}–2 and WO_{3-x}–4, thus confirming the partial persistence of the oxygen gradient even after thermal treatment. Among all samples, WO_{3-x}–8 stood out by presenting the lowest charge transfer resistance and the highest carrier density, making it the most promising candidate for application as a photoanode in green hydrogen production.

The results highlight that the careful choice of annealing conditions is crucial for either preserving or eliminating vacancy gradients, depending on the desired objective. While annealing in air favors reoxidation and structural homogenization, the use of inert atmospheres should be considered when the goal is to preserve defects and investigate their effects in isolation. In summary, this work makes significant contributions to the engineering of WO_{3-x} photoelectrodes by demonstrating the importance of precise control over deposition and post-treatment conditions as an effective strategy for optimizing their performance in solar-driven hydrogen generation.

Acknowledgments:

The authors thank the São Paulo Research Foundation (FAPESP, Grant Nos. 2022/02994-2, 2023/10449-7, and 2024/05173-5) and the National Council for Scientific and Technological Development (CNPq, Grant No. 310778/2021-2, 405522/2022-3, 407805/2023-0) for their financial support. We also appreciate the National Institute for Space Research (INPE) for providing access to SEM facilities, as well as the Aeronautics Institute of Technology (ITA), particularly the Plasma and Processes Laboratory (LPP-ITA), for their ongoing technical support and collaboration.

References

[1] S.D. Tilley, Recent Advances and Emerging Trends in Photo-Electrochemical Solar Energy Conversion, Adv Energy Mater 9 (2019) 1–13. https://doi.org/10.1002/aenm.201802877.

[2] N.S. Lewis, D.G. Nocera, Powering the planet: Chemical challenges in solar energy utilization, Proceedings of the National Academy of Sciences 103 (2006) 15729–15735. https://doi.org/10.1073/pnas.0603395103.

[3] R.M. Navarro Yerga, M. Consuelo Álvarez Galván, F. del Valle, J.A. Villoria de la Mano, J.L.G. Fierro, Water splitting on semiconductor catalysts under visiblelight irradiation, ChemSusChem 2 (2009) 471–485. https://doi.org/10.1002/cssc.200900018.

[4] O. Oruc, I. Dincer, Assessing the potential of thermochemical water splitting cycles: A bridge towards for clean and sustainable hydrogen generation, Fuel 286 (2021) 119325. https://doi.org/10.1016/j.fuel.2020.119325.

[5] Z. Chen, H.N. Dinh, E. Miller, Photoelectrochemical Water Splitting, Springer New York, New York, NY, 2013. https://doi.org/10.1007/978-1-4614-8298-7.

[6] T. Yao, X. An, H. Han, J.Q. Chen, C. Li, Photoelectrocatalytic Materials for Solar Water Splitting, 1800210 (2018) 1–36. https://doi.org/10.1002/aenm.201800210.

[7] W. Yang, R.R. Prabhakar, J. Tan, S.D. Tilley, J. Moon, Strategies for enhancing the photocurrent, photovoltage, and stability of photoelectrodes for photoelectrochemical water splitting, Chem Soc Rev 48 (2019) 4979–5015. https://doi.org/10.1039/c8cs00997j.

[8] M. Damiá N Monllor-Satoca, I. Dí Ez-Garcí, T. Lana-Villarreal, R. Gó Mez, Photoelectrocatalytic production of solar fuels with semiconductor oxides: materials, activity and modeling, 12272 | Chem. Commun 56 (2020) 12272. https://doi.org/10.1039/d0cc04387g.

[9] A. Fujishima, K. Honda, Electrochemical photolysis of water at a semiconductor electrode, Nature 238 (1972) 37–38. https://doi.org/10.1038/238037a0.

[10] Y.H. Chiu, T.H. Lai, M.Y. Kuo, P.Y. Hsieh, Y.J. Hsu, Photoelectrochemical cells for solar hydrogen production: Challenges and opportunities, APL Mater 7 (2019). https://doi.org/10.1063/1.5109785.

[11] A.K. Bhojani, M. Jha, A. Joshi, K. Bhargava, G. Singh, D.K. Singh, S. Pathak, V. Kaushik, Layered transition metal oxides (MoO3, WO3, Ga2O3, V2O5) for energy conversion and storage: A comprehensive review, J Energy Storage 107 (2025). https://doi.org/10.1016/j.est.2024.114979.

[12] M.B. Costa, M.A. de Araújo, M.V. de L. Tinoco, J.F. de Brito, L.H. Mascaro, Current trending and beyond for solar-driven water splitting reaction on WO3 photoanodes, Journal of Energy Chemistry 73 (2022) 88–113. https://doi.org/10.1016/j.jechem.2022.06.003.

[13] O. Samuel, M.H.D. Othman, R. Kamaludin, O. Sinsamphanh, H. Abdullah, M.H. Puteh, T.A. Kurniawan, WO3–based photocatalysts: A review on synthesis, performance enhancement and photocatalytic memory for environmental applications, Ceram Int 48 (2022) 5845–5875. https://doi.org/10.1016/J.CERAMINT.2021.11.158.

[14] E. Muslu, E. Eren, A.U. Oksuz, Research progress on flexible WO3 based thin film electrodes for supercapacitor applications: a comprehensive review, Emergent Mater (2024). https://doi.org/10.1007/s42247-024-00760-8.

[15] S. Gonçalves, P. Quitério, J. Freitas, D. Ivanou, T. Lopes, A. Mendes, J.P. Araújo, C.T. Sousa, A. Apolinário, Unveiling Morphology-Structure Interplay on Hydrothermal WO3 Nanoplatelets for Photoelectrochemical Solar Water Splitting, ACS Appl Mater Interfaces (2024). https://doi.org/10.1021/acsami.4c11729.

[16] Z. Ni, Q. Wang, Y. Guo, H. Liu, Q. Zhang, Research Progress of Tungsten Oxide-Based Catalysts in Photocatalytic Reactions, Catalysts 13 (2023). https://doi.org/10.3390/catal13030579.

[17] G. Hodes, D. Cahen, J. Manassen, Tungsten trioxide as a photoanode for photoelectrochemical cell (PEC), Nature 260 (1976) 312–313.

[18] R. Wang, X. Fu, Y. Guo, J. Zhang, R. Chen, X. Huang, Q. Tian, Y. Bai, WO3/g-C3N4 synergistic photocatalysts for degradation and H2 production, Ceram Int (2024). https://doi.org/10.1016/j.ceramint.2024.10.442.

[19] V. Madhavi, P. Kondaiah, H. Shaik, K.N. Kumar, T.S.S. Kumar Naik, G.M. Rao, P.C. Ramamurthy, Fabrication of porous 1D WO3 NRs and WO3/BiVO4 hetero junction photoanode for efficient

photoelectrochemical water splitting, Mater Chem Phys 274 (2021). https://doi.org/10.1016/j.matchemphys.2021.125095.

[20] J. Yadav, J.P. Singh, WO3/Ag2S type-II hierarchical heterojunction for improved charge carrier separation and photoelectrochemical water splitting performance, J Alloys Compd 925 (2022). https://doi.org/10.1016/j.jallcom.2022.166684.

[21] M. Modak, S. Rane, S. Jagtap, WO3: a review of synthesis techniques, nanocomposite materials and their morphological effects for gas sensing application, Bulletin of Materials Science 46 (2023). https://doi.org/10.1007/s12034-022-02864-5.

[22] M.H. Sayed, M.M. Gomaa, T. Imrich, R. Nebel, M. Neumann-Spallart, J. Krýsa, H. Krýsová, M. Boshta, Photoelectrochemical properties of WO3 films prepared by hydrothermal synthesis, J Photochem Photobiol A Chem 463 (2025). https://doi.org/10.1016/j.jphotochem.2024.116251.

[23] J. Feng, X. Zhao, B. Zhang, G. Yang, Q. Qian, S.S.K. Ma, Z. Chen, Z. Li, Y. Huang, Sol-gel synthesis of highly reproducible WO3 photoanodes for solar water oxidation, Sci China Mater 63 (2020) 2261–2271. https://doi.org/10.1007/s40843-020-1430-4.

[24] J. Zhang, X. Chang, C. Li, A. Li, S. Liu, T. Wang, J. Gong, WO3 photoanodes with controllable bulk and surface oxygen vacancies for photoelectrochemical water oxidation, J Mater Chem A Mater 6 (2018) 3350–3354. https://doi.org/10.1039/c7ta10056f.

[25] Y. Li, W. Zhou, D. Li, J. Xu, Multifunctional non-stoichiometric tungsten oxides: Synthesis, properties and application, J Power Sources 631 (2025). https://doi.org/10.1016/j.jpowsour.2025.236222.

[26] S. Bandi, A.K. Srivastav, Review: Oxygen-deficient tungsten oxides, J Mater Sci 56 (2021) 6615–6644. https://doi.org/10.1007/s10853-020-05757-2.

[27] R. Cheng, X. Niu, H. Li, H. Liang, P. Tsiakaras, Oxygen vacancy-rich defective tungsten oxide (WO3−x) modified by Prussian blue for efficient photocatalytic carbon dioxide conversion and tetracycline degradation, J Colloid Interface Sci 683 (2025) 807–816. https://doi.org/10.1016/j.jcis.2024.12.146.

[28] M. Brunclíková, Z. Hubička, Kment, J. Olejníček, M. Čada, P. Kšírová, J. Krýsa, Semiconducting WO3 thin films prepared by pulsed reactive magnetron sputtering, Research on Chemical Intermediates 41 (2015) 9259–9266. https://doi.org/10.1007/s11164-015-1991-8.

[29] A. Písaříková, H. Krýsová, A. Kapran, P. Písařík, M. Čada, J. Olejníček, R. Hippler, Z. Hubička, Semiconductor WO3 thin films deposited by pulsed reactive magnetron sputtering, Mater Sci Semicond Process 186 (2025) 109034. https://doi.org/10.1016/j.mssp.2024.109034.

[30] K.B. Joël-Igor N'Djoré, M. Grafouté, A. Bulou, C. Rousselot, Correlation between physical properties and electrochromic performances of DC magnetron sputtered a-WOx thin films, Materials Science and Engineering: B 290 (2023). https://doi.org/10.1016/j.mseb.2023.116261.

[31] C. Chananonnawathorn, S. Pudwat, M. Horprathum, P. Eiamchai, P. Limnontakul, C. Salawan, K. Aiempanakit, Electrochromic property dependent on oxygen gas flow rate and films thickness of sputtered WO3 films, in: Procedia Eng, Elsevier Ltd, 2012: pp. 752–758. https://doi.org/10.1016/j.proeng.2012.02.008.

[32] R. Barathy T, P.V.K. Yadav, A. Mondal, B. Ajitha, J. Jarugala, Y.A. Kumar Reddy, High porosity and oxygen vacancy enriched WO3-x thin films for room temperature hydrogen gas sensors, Int J Hydrogen Energy 50 (2024) 878–888. https://doi.org/10.1016/j.ijhydene.2023.07.218.

[33] X. Xu, M.A.P. Yazdi, R. Salut, J.M. Cote, A. Billard, N. Martin, Structure, composition and electronic transport properties of tungsten oxide thin film sputter-deposited by the reactive gas pulsing process, Mater Chem Phys 205 (2018) 391–400. https://doi.org/10.1016/j.matchemphys.2017.11.048.

[34] N.M.G. Parreira, T. Polcar, A. Cavaleiro, Characterization of W-O coatings deposited by magnetron sputtering with reactive gas pulsing, Surf Coat Technol 201 (2007) 5481–5486. https://doi.org/10.1016/j.surfcoat.2006.07.017.

[35] T. Degen, M. Sadki, E. Bron, U. König, G. Nénert, The high score suite, in: Powder Diffr, Cambridge University Press, 2014: pp. S13–S18. https://doi.org/10.1017/S0885715614000840.

[36] X. XU, Nanostructured W-O thin films by reactive sputtering: application as gas sensors, Université Bourgogne Franche-Comté, 2018.

[37] J. Olejníček, A. Hrubantová, L. Volfová, M. Dvořáková, M. Kohout, D. Tvarog, O. Gedeon, H. Wulff, R. Hippler, Z. Hubička, WO3 and WO3-x thin films prepared by DC hollow cathode discharge, Vacuum 195 (2022). https://doi.org/10.1016/j.vacuum.2021.110679.

[38] R. Azimirad, N. Naseri, O. Akhavan, A.Z. Moshfegh, Hydrophilicity variation of WO3 thin films with annealing temperature, J Phys D Appl Phys 40 (2007) 1134–1137. https://doi.org/10.1088/0022-3727/40/4/034.

[39] M. Miyauchi, M. Shibuya, Z.G. Zhao, Z. Liu, Surface wetting behavior of a WO3 electrode under light-irradiated or potential-controlled conditions, Journal of Physical Chemistry C 113 (2009) 10642–10646. https://doi.org/10.1021/jp901097b.

[40] A. Le Bail, Whole powder pattern decomposition methods and applications: A retrospection, Powder Diffr 20 (2005) 316–326. https://doi.org/10.1154/1.2135315.

[41] A. Le Bail, H. Duroy, J.L. Fourquet, Ab-initio structure determination of LiSbWO6 by X-ray powder diffraction, Mater Res Bull 23 (1988) 447–452. https://doi.org/10.1016/0025-5408(88)90019-0.

[42] M. Desseigne, N. Dirany, V. Chevallier, M. Arab, Shape dependence of photosensitive properties of WO 3 oxide for photocatalysis under solar light irradiation, Appl Surf Sci 483 (2019) 313–323. https://doi.org/10.1016/j.apsusc.2019.03.269.

[43] A. Hrubantova, R. Hippler, H. Wulff, M. Cada, J. Olejnicek, N. Nepomniashchaia, C.A. Helm, Z. Hubicka, Deposition of tungsten oxide films by reactive magnetron sputtering on different substrates, Journal of Vacuum Science & Technology A 40 (2022). https://doi.org/10.1116/6.0002012.

[44] N. Dirany, M. Arab, C. Leroux, S. Villain, V. Madigou, J.R. Gavarri, Effect of WO3 Nanoparticles Morphology on the Catalytic Properties, in: Mater Today Proc, Elsevier Ltd, 2016: pp. 230–234. https://doi.org/10.1016/j.matpr.2016.01.062.

[45] C. Shao, A.S. Malik, J. Han, D. Li, M. Dupuis, X. Zong, C. Li, Oxygen vacancy engineering with flame heating approach towards enhanced photoelectrochemical water oxidation on WO3 photoanode, Nano Energy 77 (2020). https://doi.org/10.1016/j.nanoen.2020.105190.

[46] L.D. Zhao, Q. Zhang, J. Bin Fan, L.Q. Yin, P.W. Qi, H.C. Yao, Z.J. Li, Improvement of the photoelectrochemical performance of vertically aligned WO3 nanosheet array film with a disordered surface layer by electroreduction, Journal of Solid State Electrochemistry 23 (2019) 1621–1630. https://doi.org/10.1007/s10008-019-04257-x.

[47] Ł. Haryński, A. Olejnik, K. Grochowska, K. Siuzdak, A facile method for Tauc exponent and corresponding electronic transitions determination in semiconductors directly from UV–Vis spectroscopy data, Opt Mater (Amst) 127 (2022). https://doi.org/10.1016/j.optmat.2022.112205.

[48] A. Hrubantova, R. Hippler, H. Wulff, M. Cada, J. Olejnicek, N. Nepomniashchaia, C.A. Helm, Z. Hubicka, Deposition of tungsten oxide films by reactive magnetron sputtering on different substrates, Journal of Vacuum Science & Technology A 40 (2022). https://doi.org/10.1116/6.0002012.

[49] S. Jain, A. Sanger, S. Chauhan, R. Chandra, Hydrogen sensing properties of nanostructured Pd/WO3 thin films: Role of hydrophobicity during recovery process, Mater Res Express 1 (2014). https://doi.org/10.1088/2053-1591/1/3/035046.

[50] C.G. Granqvist, Handbook of Inorganic Electrochromic Materials, Elsevier Science, 1995. https://doi.org/https://doi.org/10.1016/B978-0-444-89930-9.X5000-4.

[51] Y. Liu, L. Kong, X. Guo, J. Xu, S. Shi, L. Li, Surface oxygen vacancies on WO3 nanoplate arrays induced by Ar plasma treatment for efficient photoelectrochemical water oxidation, Journal of Physics and Chemistry of Solids 149 (2021). https://doi.org/10.1016/j.jpcs.2020.109823.

[52] J. Liu, S.M. Xu, Y. Li, R. Zhang, M. Shao, Facet engineering of WO3 arrays toward highly efficient and stable photoelectrochemical hydrogen generation from natural seawater, Appl Catal B 264 (2020). https://doi.org/10.1016/j.apcatb.2019.118540.

[53] J. Zhang, P. Zhang, T. Wang, J. Gong, Monoclinic WO3 nanomultilayers with preferentially exposed (002) facets for photoelectrochemical water splitting, Nano Energy 11 (2015) 189–195. https://doi.org/10.1016/j.nanoen.2014.10.021.

[54] Y. Wang, W. Tian, C. Chen, W. Xu, L. Li, Tungsten Trioxide Nanostructures for Photoelectrochemical Water Splitting: Material Engineering and Charge Carrier Dynamic Manipulation, Adv Funct Mater 29 (2019). https://doi.org/10.1002/adfm.201809036.